Evidence of Small Scale Plasma Irregularity Effects on Whistler Mode Chorus Propagation

Poorya Hosseini[1], Oleksiy Agapitov[2], Vijay Harid[1], and Mark Gołkowski[1]

[1]Department of Electrical Engineering, University of Colorado Denver, Denver, CO, USA.

[2]Space Sciences Laboratory, University of California, Berkeley, CA, USA.

Abstract

The impact of randomly distributed field-aligned density irregularities on whistler-mode wave propagation is investigated using full-wave simulations and multi-point spacecraft observations. The irregularities are modeled as randomized density perturbations between 1-10% of the nominal background density value with scales of ~10-60 km transverse and ~50-500 km along the background magnetic field. The density irregularities affect whistler wave propagation and lead to spatial modulation of wave average power density accompanied by spreading of the wave normal angle distribution. Wave power variation is shown to statistically increase with the depth of density irregularities. The simulation results are in good agreement with the observed correlations of chorus power and variation of the plasma density from multi-point observations by the four MMS spacecraft. The change in fundamental wave properties from scattering from these irregularities affects the efficiency of wave-particle interactions in the radiation belts and needs to be incorporated into large-scale energetic-particle flux models.

Plain Language Summary

Electromagnetic waves in the near-Earth space environment are a major contributor to space weather processes that can affect a large array of technological platforms in space and on the ground. A key class of waves in near-Earth space are so called whistler mode waves and it is important to accurately model and predict how these waves propagate. Whistler mode wave propagation is affected by the background plasma and in this work we simulate propagation of these waves in the presence of small scale (smaller than a wavelength) irregularities of the plasma medium. Past simulations of these waves have focused on a smooth background or very large plasma density structures. We simulate small structures and compare our results to observations made with multiple spacecraft that fly in close formation. Agreement between the simulations and observations suggests that the plasma density in near-Earth space may be filled with many small irregularities that need to be taken into account.

I. Introduction

Whistler mode chorus waves are intense electromagnetic waves in the Earth's magnetosphere and a key driver of radiation belt dynamics (Bortnik and Thorne, 2007; Horne et al., 2005; Thorne, 2010; Ni et al., 2008; Hosseini et al., 2019, Tsurutani & Smith, 1974). These waves are generated by a non-linear cyclotron resonance interaction (Sudan and Ott, 1971; Nunn, 1974; Bell 1984; Omura et al., 2008, 2009; Hikishima and Omura, 2010; Katoh and Omura, 2016; Ke et al., 2017; Golkowski and Gibby, 2017; Golkowski et al., 2019; and references therein) in the close vicinity of the geomagnetic equator (Santolik et al., 2004, LeDocq et al., 1998).

In order to model the effects of chorus waves on energetic particles accurately, it is critical to know the locations and spatial scales of the wave power distribution as these determine the applicability of quasi-linear and nonlinear approaches (Bell and Inan, 1981; Albert, 2002; Artemyev et al., 2015, 2016; Zhang et al., 2020; Allanson et el., 2020; Gan et al., 2020). Therefore, quantifying both the spatial extent of individual chorus wave packets and the propagation of such packets away from the source region is required. In this study we focus on lower band chorus as it is known to be more prevalent and intense (Haque et al., 2011; Santolík et al., 2010). Close to the source in the dawn and day region, the spatial extent of a single chorus element transverse to the background magnetic field has been found to be ~ 600-800 km (Santolik and Gurnett, 2003; Agapitov et al., 2017, 2019; Shen et al., 2019). This chorus source scale demonstrates good correspondence to the spatial scales of discrete localized pulsating auroral events (Nishimura et al., 2010, 2011). However, chorus induced phenomena are also known to exist on smaller scales of ~100-300 km, such as electron microbursts (Breneman et al., 2017; Mozer et al., 2018; Shumko et al., 2018, 2020; Crew et al., 2016). Moreover, statistics of wave normal angle (WNA) distributions show chorus waves predominantly propagate close to parallel to geomagnetic field lines up to mid-latitudes (Agapitov et al., 2012, 2013), which is not consistent with propagation in a homogenous or smooth background where oblique waves are predicted from raytracing (Breuillard et al., 2012). The unexpected changes in wave parameters and scale size that transpire between the equatorial source and other locations in the magnetosphere are not well explained. It is possible that such changes result from a combination of factors such as inhomogeneity of the hot electron distribution in the source region, selective amplification (Santolik et al., 2009; Haque et al., 2010; Agapitov et al., 2013; Li et al. 2013, Santolik et al. 2014), or nuances of Landau damping of oblique waves (Hsieh & Omura, 2018).

However, the linear phenomena of propagation in a highly inhomogeneous cold plasma medium can also cause such features.

Past studies on the effect of cold plasma irregularities on whistler waves have mostly focused on either a smooth plasma background with no irregularities, or well-defined duct-like structures that extend along the entire field line between conjugate ionospheres (Thomson, 1978; Karpman and Kaufman, 1981; Koons, 1989; Maxworth et al., 2020). Direct measurements of whistler mode waves propagating in large scale field aligned irregularities are rare (Smith and Angerami 1968; Sonwalkar et al. 1994; Sonwalkar 2006) and the bulk of evidence for elongated duct structures is indirect, for example ground observations of chorus waves (Gołkowski and Inan, 2008; Hosseini at al., 2017). Two direct observations of plasma irregularities that do extend to ionospheric altitudes worth mentioning are Z-mode echoes on the IMAGE satellite (Carpenter et al., 2003; Sonwalkar et al., 2011) and imaging with the Murchison Widefield Array radio telescope (Loi et al., 2015). While such large scale ducts extending from ionosphere to conjugate ionosphere likely play a role in guiding whistler waves inside the plasmasphere, much smaller irregularities have recently seen targeted investigations. Using cross correlation of observables on multiple spacecraft, Agapitov et al. (2011) reported the parameters of plasma density fluctuation scales to be ~60-100 km transverse to and 1000-1500 km along the background magnetic field. Hanzelka and Santolik (2019) investigated the guiding effects of field aligned density irregularities with only 6% density changes. These field aligned irregularities were made narrow in the transverse direction and a key finding was that the presence of such "weak" and "thin" ducts can explain observed wave parameters and such structures are likely more prevalent than previously thought.

The majority of all past work on wave propagation modeling, including the recent Hanzelka and Santolik (2019) study, has been based on raytracing and therefore limited to scenarios where density changes slowly over a wavelength. The impact of smaller structures can only be addressed with a full-wave analysis. We present a full-wave model to study the effects of whistler wave propagation in the plasmasphere with randomized plasma fluctuations. The parameters of plasma density fluctuations modeled are based on the estimates of Agapitov et al. (2011) and then compared with wave and plasma measurements on the Magnetosphere Multi-Scale (MMS) project (Burch et al., 2016; Fuselier et al., 2016; Pollock et al., 2016).

II. The full-wave model

A two dimensional finite difference time domain (FDTD) scheme is used to solve Maxwell's equations and the linearized cold-fluid equations, where ions are immobile and the electrons are modeled as a zero temperature and collision-free fluid (Helliwell, 1965; Stix, 1992; Gordeev et al., 1994).

$$\frac{\partial \mathbf{J}}{\partial t} = \frac{q^2 N_0}{m}\mathbf{E} - \frac{q}{m}\mathbf{J} \times \mathbf{B}_0$$

$$\nabla \times \mathbf{E} = -\frac{\partial \mathbf{B}}{\partial t} \qquad \nabla \times \mathbf{B} = \mu_0 \mathbf{J} + \mu_0 \varepsilon_0 \frac{\partial \mathbf{E}}{\partial t}$$

where ε_0 is the vacuum permittivity; μ_0 is the vacuum permeability; m and $q > 0$ are the electron mass and charge, respectively; $c = \frac{1}{\sqrt{\mu_0 \varepsilon_0}}$ is the speed of light in vacuum; $\mathbf{J}$ is the electron current, and N_0 is the initial electron density. The electron current term under the cold linearized approximation is defined as $\mathbf{J} = -\boldsymbol{q N_0 u}$ where $\boldsymbol{u}$ is the cold electron fluid velocity (Yoon, 2011). The fields **E**, **B**, and **J** are regarded as three-dimensional vector quantities. We consider a model with a constant ambient magnetic field $\mathbf{B}_0$ in the z direction ($\mathbf{B}_0 = B_{0z}\hat{z}$). This propagation model has similarity to that presented by Streltsov *et al.* (2006, 2007) but we do not neglect the displacement current. Neglecting the displacement current results in the quasi-longitudinal approximation which has validity up to near the resonance cone (Helliwell, 1965). We also investigate much smaller scale irregularities than were considered by Streltsov et al. (2007). Woodroffe and Streltsov (2014) investigated sub-wavelength irregularities in the ionosphere, whereas the focus here is the magnetosphere. Full wave modeling of whistler mode waves was also presented by Katoh (2014) but with consideration of long field aligned ducts.

We utilize a two-dimensional (2-D) Cartesian geometry and spatial inhomogeneity of the cold plasma density in both the x and z directions. The ambient magnetic field strength, $B_0 = 263.5\ nT$ (i.e.,$f_c = 7.45$ kHz), is chosen to correspond to the geomagnetic field at ~5°-latitude at L =4.9 using a dipole model. The unperturbed background plasma density is chosen as $N_0 = 20\ cm^{-3}$, typical for a chorus source region just outside the plasmapause [Carpenter and Anderson, 1992]. The density irregularities are incorporated by adding a perturbation to the background cold plasma density:

$$N(x,z) = N_0 \pm \delta N \times D_0(x,z)$$

where δN is the nominal magnitude of density fluctuation while $D(x,z)$ corresponds to the spatial profile centered at (x_0, z_0)

$$D_0(x,z) = exp\left(-\left(\frac{x-x_0}{dx}\right)^2 - \left(\frac{z-z_0}{dz}\right)^2\right).$$

The quantity dx (dz) is the fluctuation's size across (along) the geomagnetic field. In contrast to previous studies (Streltsov et al., 2007; Woodroffe and Streltsov, 2013), we focus here on arbitrarily distributed small-sized density irregularities as reported by Agapitov et al. (2011). A medium consisting of such density irregularities can be generated by adding a number of small-scale fluctuations with randomized parameters as follows:

$$N(x,z) = N_0 \pm \delta N \times \sum_{i=1}^{n} D_i(x,z)$$

where n is the total number of irregularities. This procedure yields a fixed set of irregularities with randomized (normal distribution) scale sizes (dx, dz) centered around randomized (uniform distribution) locations (x_i, z_i). Figure 1a shows an example of randomized density irregularities with $n = 50$, $dx = 60$ km, $dz = 500$ km and Figure 2a shows an example of randomized density irregularities with $n = 50$, $dx = 10$ km, $dz = 50$ km. With our procedure it is possible that the irregularities created would land on top of each other at the same location, but we have selected cases where the generated irregularities are isolated from each other. We target our investigation to assess the effect of the size and depth of the irregularities on wave propagation.

The electric and magnetic fields **E** and **B** as well as the current density **J** are calculated at each time step on a staggered Yee grid (Taflove and Hagness, 2005). The spatial steps $\Delta x = 0.94$ km and $\Delta z = 1.00$ km resolve the wavelength ($\lambda \approx 15$ km) and are much smaller than the scale sizes of the irregularities. The time and spatial steps must satisfy a CFL stability criterion taken here as $\Delta t \leq \frac{1}{c\sqrt{\Delta x^{-2}+\Delta z^{-2}}}$, which is over restrictive since the whistler mode propagation speed is much less than *c* (Gedney, 2011). The time step is thus calculated as $\Delta t = 2.06\mu s$, and is much smaller than the electromagnetic field oscillation period, $f^{-1} = 670.8\mu s$. A whistler wave of chosen frequency $f = 0.2f_c = 1.49$ kHz is injected in the middle of the simulation domain ($z_s = 1000$ km) using a source that is spatially limited in the *x* direction via the expression, $D(x) = \frac{1}{2}\left[\tanh\left(\frac{x+285\ km}{57\ km}\right) - \tanh\left(\frac{x-285\ km}{57\ km}\right)\right]$.

The source mimics an equatorial chorus element that has Poynting flux initially directed primarily along the field line. The model utilizes a perfect electrical conductor (PEC) surface at

the boundary of the simulation space and the simulation is terminated before the initial wavefront reaches the boundaries.

III. Simulation Results

The full wave simulations are run under several density configurations to find correlations between whistler-wave fields and the density irregularities. The entire simulation domain is $1000\ \text{km} \times 2000\ \text{km}$ and we consider small (dx =10 km, dz = 50 km), medium (dx =30 km, dz = 250 km) and large (dx =60 km, dz = 500 km) density irregularities with $n = 50$ and δN values of 1%, 5%, and 8%. We examine the effect on the variation of wave magnitude, B_w from that of the smooth case with no irregularities. Figure 1 shows the results for the large scale irregularities (corresponding to scale size inferred from Cluster observations, see Figure 4 of Agapitov et al., (2011)) and Figure 2 shows the results for the small scale irregularities. In both figures panels (b)-(d) show the wave amplitude profile at a snapshot in time ($t = 0.02\ \text{s}$) for density fluctuations of 1%, 5%, and 8%, respectively. The wave amplitude at $z = 350\ \text{km}$ (at the left boundary of the domain) is shown with the blue curve in panels (e)-(g). Additionally, the integrated density change that the wave has propagated through from the source located at $z = 1000\ \text{km}$ to $z = 350\ \text{km}$ is shown with a red curve. Wave amplitude is seen to fluctuate in correspondence with the integrated (not local) density change along the propagation direction and in proportion to the depth of the irregularities, since the depth is proportional to the plasma gradients that guide the waves. The integrated density is a crude but still useful estimate of the path taken by the wave, and it can be seen the wave amplitude can be increased up to threefold. The deepest 8% density fluctuations produce the largest changes in wave amplitude. The wave electric field (shown in supporting information S2) is also amplified in the density enhancements. The WNA (shown in S2) is more parallel where wave amplitude is enhanced.

The irregularities lead to considerable focusing of wave power denisty that is observable even after the wave has propagated away from an irregularity. Here we emphasized the focusing effect due to the density enhancements. However, density depletions also have defocusing (dispersive) effect on the wave power (shown in S3).

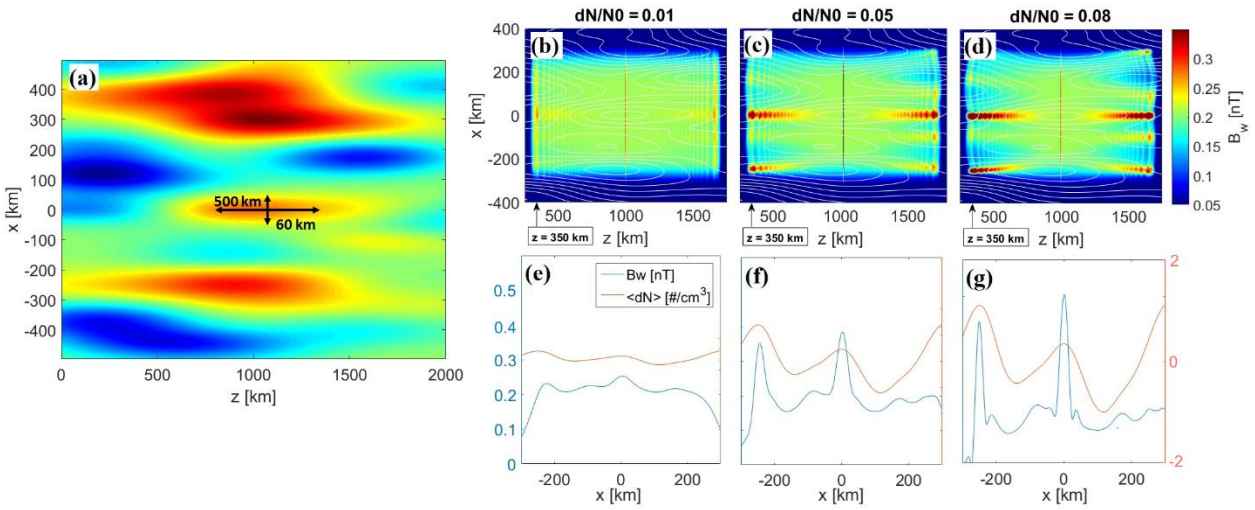

Figure 1. a) Plasma density profile for the irregularities with sizes $dx = 60$ km and $dz = 500$ km ($n = 50$). The color scale of panel (a) is arbitrary since the depth of the irregularities changes for cases considered in (b-g). Wave amplitude profile at a snapshot in time ($t = 0.02$ s) for density variations b) 1%, c) 5%, and d) 8% of the background. The wave amplitude at $z = 350$ km (at the left boundary of the domain) is shown with the blue curve in panels (e)-(g) with the integrated density change that the wave has propagated through with a red curve.

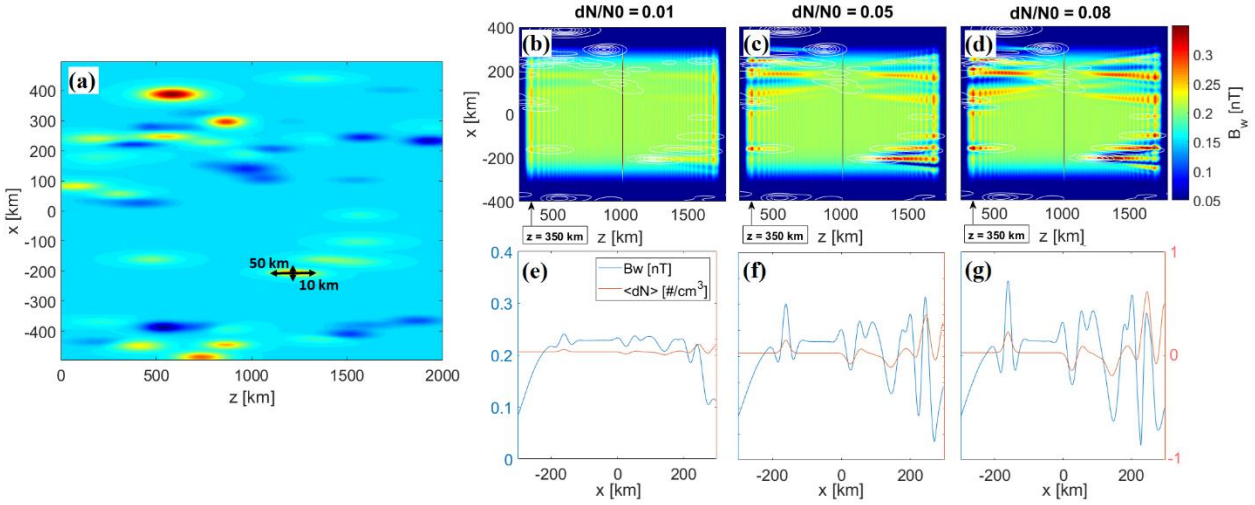

Figure 2. a) Plasma density profile for the irregularities with sizes of $dx = 10$ km and $dz = 50$ km ($n = 50$). The color scale of panel (a) is arbitrary since the depth of the irregularities changes for cases considered in (b-g). Wave amplitude profile for density fluctuations that vary b) 1%, c) 5%, and d) 8% of the background. The wave amplitude at $z = 350$ km (at the left boundary of the domain) is shown with the blue curve in panels (e)-(g) with the integrated density change that the wave has propagated through with a red curve.

Figure 3 shows the compiled results for the three density irregularity sizes and for the three different values of the density modulation level δN (1%, 4%, 8%). The change in wave magnetic field (compared to the unperturbed case Bw_0) versus the density change (compared to the ambient N_0) are shown. The horizontal range bars show the observed variation in normalized

density change ($\frac{dN}{N_0}$). The vertical range bar is the variation in wave amplitude change ($\frac{dBw}{Bw_0}$) compared to the unperturbed case. Note that although δN is set as an input parameter 1%, 4%, 8%), the actual fluctuations in density (dN) will have a finite range around this due to adjacency of irregularities. Two general trends are observed, variation in wave amplitude increases with irregularity size (dx, dz) and also depth of the irregularities (δN).

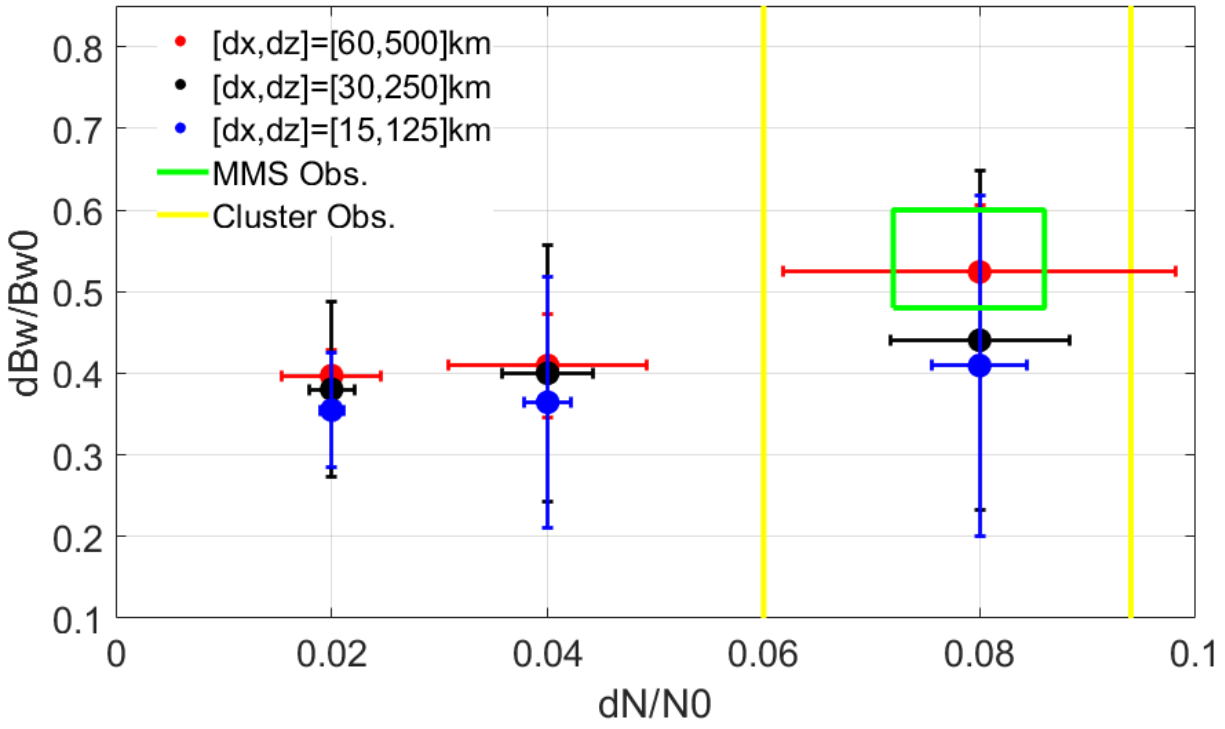

Figure 3. Normalized change in wave magnetic field compared to the unperturbed case (B_{w0}) is directly related to the normalized density change (compared to the ambient N_0). Simulation results for δN = 1%, 4%, and 8% are shown. Horizontal range bars indicate the measured variations in density, which can be different from δN due to adjacency of irregularities. Vertical range bars indicate variation of the wave amplitude at $z = 350$ km. The green rectangle shows the range of parameters derived from MMS observations. The area bounded by yellow lines shows the Cluster density observation ranges.

IV. Comparison of Simulation Results with Spacecraft Observations

Direct validation of the simulation results requires a very compact configuration of multi-point spacecraft, on the order of the transverse scale of the plasma irregularities (~5-100 km), and with better than 1-s cadence of wave and density observations. Also, a comparison is only possible when the effects from other processes (wave amplification/damping and/or hot plasma inhomogeneities in the source) are negligible. As a result, a rigorous comparison of wave

amplitude modulation between the simulation and the Cluster observations of Agapitov et al., (2011) is difficult as the inter-spacecraft distance along the magnetic field was from 70 to 260 km and plasma density measurements were made with a ~4-s cadence. However, Agapitov et al., (2011) analyzed the wave phase cross-correlation and the results are in a good agreement with the observed plasma irregularities. To validate the simulation results presented in Section 3, we use the multi-point measurements of chorus type whistler waves from the four identically equipped MMS spacecraft at higher L-shell but affected by a similar level of plasma density fluctuation. The MMS mission has high-time-resolution plasma and wave instruments (Burch et al., 2016; Fuselier et al., 2016). We used the ion distributions and moments from the Fast Plasma Investigation (FPI) (Pollock et al., 2016), the background magnetic field from the Fluxgate Magnetometer (FGM) (Russell et al., 2016; Torbert et al., 2016), and wave magnetic field from the Search Coil Magnetometer (LeContel et al., 2016).

The four MMS spacecraft observed chorus wave activity during more than 2 hours (0130-0400UT) on June 19, 2018, and high-resolution (8192 s^{-1}) waveforms were collected during ~10 minutes, with ~3 minutes of simultaneous plasma density measurements (with 150 ms time resolution) in the burst regime (03:23-03:26 UT ~4:47 MLT). The spacecraft were located at L~7.41 at a geomagnetic latitude of 3.8 degrees (~4000 km above the equator plane). MMS doesn't provide burst measurements in the inner magnetosphere on a regular basis, and this interval was identified as the most relevant to the parameters of the numerical model. The distance between individual MMS probes ranged from 15 km to 150 km at the time of observation. Specifically, the four spacecraft were almost in a plane perpendicular to the geomagnetic field. MMS3 and MMS4 were the closest to each other and separated by only ~10-12 km (which allows for neglecting of wave damping/amplification effects between spacecraft), MMS2 was ~150 km from this pair and MMS1 was in between at ~95-110 km from the MMS3,4 pair and at 50-60 km from MMS2 (shown in S1). MMS1 recorded a localized depression of plasma density of ~8% of background passing through the spacecraft. The density estimates are based on FPI ion measurements.

All four spacecraft recorded chorus waves series during 50 seconds (Figure 4a-d) with maximal amplitudes above 1 nT captured by MMS1. The dynamic spectra of wave activity presented in Figure 4e-h show that the temporal structure of perturbations was observed to be very similar by all four spacecraft and the same chorus elements were observed by all spacecraft

but with different amplitude. This is reflected in the high correlation coefficient estimated making use of time series of wave power around the frequency maximum (~700 Hz) from the different spacecraft (Figure 4i). The slow decay of the correlation coefficient from 0.97 to 0.85 with inter-spacecraft distance increase from 10 km to 145 km is in agreement with the dependence obtained from the Van Allen Probes and THEMIS measurements at distances from 150 km to 800 km (Agapitov et al., 2017; 2019). MMS1 solely observed a significant depletion of wave power at 03:23:35-03:23:43. This perturbation of wave amplitude is accompanied by perturbation of WNA, θ, distribution: the observed waves are predominantly quasi-parallel with $\theta < 20°$ (Figure 4j), however, during the observed reduction of wave amplitude on MMS1 the distribution of θ became significantly more oblique (Figure 4k) indicating perturbations of the wave front.

As was shown in Section 3, the whistler wave front can be perturbed and wave amplitude can be spatially modulated (focused/defocused) by variations in the cold plasma density. The plasma density during the processed interval (Figure 4l) was about 3.2 cm^{-3} with fast (non-correlated even at the closest spacecraft) fluctuations of about 1% and slower fluctuations of about 5-7% with the spatial scale of about 50-100 km (similar to the estimations of Agapitov et al., (2011)), and similar to the parameters used for the numerical model result obtained in Figure 1. Since the four spacecraft were spaced closely along the background magnetic field (the maximal distance along B_0 was less than 50 km), the field-aligned scale of density fluctuation couldn't be determined directly. Estimation based on the time of observation of the density depletion and field-aligned velocity (~50 km/s) gives ~500 km for the parallel scale. The decrease of wave amplitude recorded only by MMS1 coincides with a local (observed only by MMS1) plasma density decrease. The localization of the density depletion is seen in Figure 4m, where density differences between different MMS spacecraft are shown. The density variation was in the range of 5-8% with the minimal value ~0.9 of the background. The wave amplitude ratio together with density ratio is presented in Figure 4n-t (the density is 4-s shifted). The density depletion is 4-s second ahead of the effects in the wave amplitude indicating propagation of the density depletion (~50 km/sec) -along the background magnetic field to the geomagnetic equator – the effects in the wave amplitude are maximal when the entire plasma depletion cell is on the wave path from the equator to the spacecraft. The wave amplitude recorded by MMS1 decreases ~2 times (dB_w/B_{w0} is ~50%) but MMS2,3,4 observations do not show significant changes which

indicates that the effect is local and caused by the observed density depletion. The comparison with the numerical results is presented in Figure 3. The range of variation of the density and the wave amplitude is marked with a green rectangle, signifying that the density depletion/enhancements between 5% and 8% and irregularity scales sizes of ~60 km transverse and ~500 km parallel are expected.

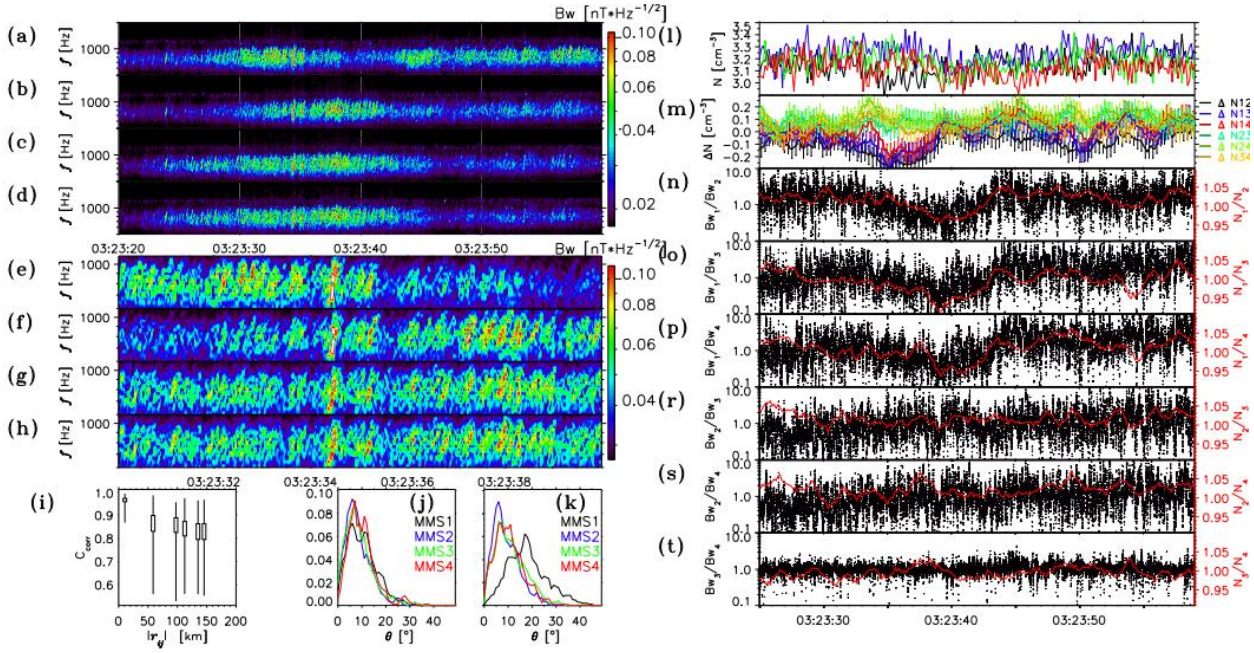

Figure 4. Magnetic field dynamic spectrum based on magnetic field VLF waveform measurements by the four MMS spacecraft on June 19, 2018 (a-d). The structure of chorus is shown in a shorter time scale (e-h). (i) – the correlation coefficient where boxes show the distribution of the average values (95% confidence interval) and the error bars indicate the +/- 2 std. range of the correlation coefficient distribution. (j,k) – WNA distributions before (03:23:30-03:23:34) and during the decrease of wave power on MMS1 (03:23:34-03:23:39). (l) – plasma density from the four spacecraft. (m) – relative differences of plasma density between the MMS spacecraft pairs. (n-t) – wave amplitude ratios from the pairs of MMS spacecraft (the black dots) and the corresponding ratios of plasma density shown with the red curve (the density is 4-s shifted).

V. Conclusion

We sought to address the fact that many chorus observations a few degrees in latitude from the equatorial source region and at mid latitudes are not consistent with propagation in a homogeneous background density nor with the scenario of very large and relatively deep (>10%) enhancement/depletion ducts. We quantified the effect of wavelength and sub wavelength sized plasma irregularities with depletions of <10%. Such irregularities are difficult to measure

directly but have been successfully inferred indirectly using wave coherence analysis on the Cluster spacecraft (Agapitov et al., 2011). In a full wave numerical study we quantified that small scale plasma density fluctuations lead to fluctuations of wave amplitude across the wave front. Specifically, a ~8% (dN/N_0) density fluctuation leads to a ~50% ($dB\mathrm{w}/B\mathrm{w}_0$) wave amplitude. This relationship between density changes and wave amplitude fluctuations is further confirmed with MMS observations. Wavelength and subwavelength irregularities may be a common feature near the chorus source region, especially following erosion of the plasmapause boundary (LeDocq et al., 1994). The primary effect of such small scale irregularities is to focus wave power density and create local hot spots of high wave amplitude and near parallel-WNA. Since the wave amplitude exhibits increased spatial variation, care must be taken in averaging of wave amplitudes for input into radiation belt models. The local hotspots of high wave amplitude will be favorable for nonlinear interactions and may explain small scale phenomena such as microbursts or facilitate the nonlinear chorus generation process.

Acknowledgment

This work was funded by NASA grant 80NSSC19K0264. O.A. was partially supported by NASA grants 80NNSC19K0848, 80NSSC20K0218, and NSF grant NSF 1914670. The wave and plasma measurements from the Magnetosphere Multi-Scale (MMS) mission can be found on https://lasp.colorado.edu/mms/sdc/public/data/. The French LPP involvement for the SCM instrument is supported by CNES and CNRS. The simulation data used to plot the presented figures is in the supporting documents. More details on the numerical full-wave model can be requested from Hosseini. P. (poorya.hosseini@ucdenver.edu).

References:

Agapitov, O., Krasnoselskikh, V., Dudok de Wit, T., Khotyaintsev, Y., Pickett, J. S., Santolík, O., & Rolland, G. (2011). Multispacecraft observations of chorus emissions as a tool for the plasma density fluctuations' remote sensing. Journal of Geophysical Research: Space Physics, 116(A9).

Agapitov, O., Krasnoselskikh, V., Khotyaintsev, Y. V., & Rolland, G. (2012). Correction to "A statistical study of the propagation characteristics of whistler waves observed by Cluster" Geophysical research letters, 38(20).

Agapitov, O., Artemyev, A., Krasnoselskikh, V., Khotyaintsev, Y. V., Mourenas, D., Breuillard, H., ... & Rolland, G. (2013). Statistics of whistler mode waves in the outer radiation belt:

322 Cluster STAFF-SA measurements. Journal of Geophysical Research: Space Physics, 118(6),
323 3407-3420.
324 Agapitov, O., Blum, L. W., Mozer, F. S., Bonnell, J. W., & Wygant, J. (2017). Chorus whistler
325 wave source scales as determined from multipoint Van Allen Probe measurements.
326 Geophysical Research Letters, 44(6), 2017GL072701.
327 Agapitov, O., Mourenas, D., Artemyev, A., Hospodarsky, G., & Bonnell, J. W. (2019). Time
328 scales for electron quasi-linear diffusion by lower-band chorus waves: The effects of ωpe/Ωce
329 dependence on geomagnetic activity. Geophysical Research Letters, 46(12), 6178-6187.
330 Albert, J. M. (2002). Nonlinear interaction of outer zone electrons with VLF waves. Geophysical
331 research letters, 29(8), 116-1.
332 Allanson, O., Watt, C. E., Ratcliffe, H., Allison, H. J., Meredith, N. P., Bentley, S. N., ... &
333 Glauert, S. A. (2020). Particle-in-cell experiments examine electron diffusion by whistler-
334 mode waves: 2. Quasilinear and nonlinear dynamics. Journal of Geophysical Research: Space
335 Physics.
336 Artemyev, A. V., Agapitov, O. V., Mourenas, D., Krasnoselskikh, V. V., & Mozer, F. S. (2015).
337 Wave energy budget analysis in the Earth's radiation belts uncovers a missing energy. Nature
338 communications, 6, 7143.
339 Artemyev, A., Agapitov, O., Mourenas, D., Krasnoselskikh, V., Shastun, V., & Mozer, F.
340 (2016). Oblique whistler-mode waves in the Earth's inner magnetosphere: Energy
341 distribution, origins, and role in radiation belt dynamics. Space Science Reviews, 200(1-4),
342 261-355.
343 Bell, T. F., & Inan, U. S. (1981). Transient nonlinear pitch angle scattering of energetic electrons
344 by coherent VLF wave packets in the magnetosphere. Journal of Geophysical Research:
345 Space Physics, 86(A11), 9047-9063.
346 Bell, T. F. (1984). The nonlinear gyroresonance interaction between energetic electrons and
347 coherent VLF waves propagating at an arbitrary angle with respect to the Earth's magnetic
348 field. Journal of Geophysical Research: Space Physics, 89(A2), 905-918.
349 Bortnik, J., & Thorne, R. M. (2007). The dual role of ELF/VLF chorus waves in the acceleration
350 and precipitation of radiation belt electrons. Journal of Atmospheric and Solar-Terrestrial
351 Physics, 69(3), 378-386.

352 Burch, J. L., Moore, T. E., Torbert, R. B., & Giles, B. L. (2016). Magnetospheric multiscale
353 overview and science objectives. Space Science Reviews, 199(1-4), 5-21.
354 Breneman, A. W., Crew, A., Sample, J., Klumpar, D., Johnson, A., Agapitov, O., et al. (2017).
355 Observations Directly Linking Relativistic Electron Microbursts to Whistler Mode Chorus:
356 Van Allen Probes and FIREBIRD II. Geophysical Research Letters, 2017GL075001.
357 Breuillard, H., Zaliznyak, Y., Krasnoselskikh, V., Agapitov, O., Artemyev, A., & Rolland, G.
358 (2012). Chorus wave-normal statistics in the Earth's radiation belts from ray tracing
359 technique.
360 Carpenter, D. L., and R. R. Anderson (1992), An ISEE/whistler model of equatorial electron
361 density in the magnetosphere,J. Geophys. Res.,97,1097–1108.
362 Carpenter, D. L., Bell, T. F., Inan, U. S., Benson, R. F., Sonwalkar, V. S., Reinisch, B. W., &
363 Gallagher, D. L. (2003). Z-mode sounding within propagation “cavities” and other inner
364 magnetospheric regions by the RPI instrument on the IMAGE satellite. Journal of
365 Geophysical Research: Space Physics, 108(A12).
366 Crew, A. B., Spence, H. E., Blake, J. B., Klumpar, D. M., Larsen, B. A., O’Brien, T. P., et al.
367 (2016). First multipoint in situ observations of electron microbursts: Initial results from the
368 NSF FIREBIRD II mission. Journal of Geophysical Research: Space Physics, 121(6),
369 2016JA022485.
370 Fuselier, S. A., Lewis, W. S., Schiff, C., Ergun, R., Burch, J. L., Petrinec, S. M., & Trattner, K. J.
371 (2016). Magnetospheric multiscale science mission profile and operations. Space Science
372 Reviews, 199(1-4), 77-103.
373 Gan, L., Li, W., Ma, Q., Albert, J. M., Artemyev, A. V., & Bortnik, J. (2020). Nonlinear
374 Interactions Between Radiation Belt Electrons and Chorus Waves: Dependence on Wave
375 Amplitude Modulation. Geophysical Research Letters, 47(4), e2019GL085987.
376 Gedney, S. D. (2011). Introduction to the finite-difference time-domain (FDTD) method for
377 electromagnetics. Synthesis Lectures on Computational Electromagnetics, 6(1), 1-250.
378 Gołkowski, M., & Inan, U. S. (2008). Multistation observations of ELF/VLF whistler mode
379 chorus. Journal of Geophysical Research: Space Physics, 113(A8).
380 Gołkowski, M., & Gibby, A. R. (2017). On the conditions for nonlinear growth in
381 magnetospheric chorus and triggered emissions. Physics of Plasmas, 24(9), 092904.

Gołkowski, M., Harid, V., & Hosseini, P. (2019). Review of Controlled Excitation of Non-linear Wave-Particle Interactions in the Magnetosphere. Frontiers in Astronomy and Space Sciences, 6, 2.a

Gordeev, A. V., Kingsep, A. S., & Rudakov, L. I. (1994). Electron magnetohydrodynamics. Physics Reports, 243(5), 215-315.

Hanzelka, M., & Santolík, O. (2019). Effects of ducting on whistler mode chorus or exohiss in the outer radiation belt. Geophysical Research Letters, 46(11), 5735-5745.

Haque, N., Spasojevic, M., Santolík, O., & Inan, U. S. (2010). Wave normal angles of magnetospheric chorus emissions observed on the Polar spacecraft. Journal of Geophysical Research: Space Physics, 115(A4).

Haque, N., Inan, U. S., Bell, T. F., Pickett, J. S., Trotignon, J. G., & Facskó, G. (2011). Cluster observations of whistler mode ducts and banded chorus. Geophysical Research Letters, 38(18), L18107.

Helliwell, R. A. (1965). Whistlers and related ionospheric phenomena (Vol. 50, p. 406). Stanford, Calif.: Stanford University Press.

Hikishima, M., Omura, Y., & Summers, D. (2010). Self-consistent particle simulation of whistler mode triggered emissions. Journal of Geophysical Research: Space Physics, 115(A12).

Horne, R. B., Thorne, R. M., Glauert, S. A., Albert, J. M., Meredith, N. P., & Anderson, R. R. (2005). Timescale for radiation belt electron acceleration by whistler mode chorus waves. Journal of Geophysical Research: Space Physics, 110(A3).

Hosseini, P., M. Gołkowski, and D. L. Turner (2017), Unique concurrent observations of whistler mode hiss, chorus, and triggered emissions, J. Geophys. Res. Space Physics, 122,6271–6282, doi:10.1002/2017JA024072.

Hosseini, P., Gołkowski, M., & Harid, V. (2019). Remote sensing of radiation belt energetic electrons using lightning triggered upper band chorus. Geophysical Research Letters, 46(1), 37-47.

Hsieh, Y. K., & Omura, Y. (2018). Nonlinear damping of oblique whistler mode waves via Landau resonance. Journal of Geophysical Research: Space Physics, 123(9), 7462-7472.

Karpman, V. I., & Kaufman, R. N. (1981). Whistler detrapping from a density crest duct. Physics Letters A, 84(1), 9–12.

412 Koons, H. C. (1989). Observations of large-amplitude, whistler mode wave ducts in the outer
413 plasmasphere. Journal of Geophysical Research: Space Physics, 94(A11), 15393–15397.
414 Katoh, Y. (2014). A simulation study of the propagation of whistler-mode chorus in the Earth's
415 inner magnetosphere. Earth, Planets and Space, 66(1), 6.
416 Katoh, Y., & Omura, Y. (2016). Electron hybrid code simulation of whistler-mode chorus
417 generation with real parameters in the Earth's inner magnetosphere. Earth, Planets and Space,
418 68(1), 192.
419 Ke, Y., Gao, X., Lu, Q., Wang, X., & Wang, S. (2017). Generation of rising-tone chorus in a
420 two-dimensional mirror field by using the general curvilinear PIC code. Journal of
421 Geophysical Research: Space Physics, 122(8), 8154-8165.
422 Le Contel, O., Leroy, P., Roux, A., Coillot, C., Alison, D., Bouabdellah, A., ... & Torbert, R. B.
423 (2016). The search-coil magnetometer for MMS. Space Science Reviews, 199(1-4), 257-282.
424 LeDocq, M. J., Gurnett, D. A., & Anderson, R. R. (1994). Electron number density fluctuations
425 near the plasmapause observed by the CRRES spacecraft. Journal of Geophysical Research:
426 Space Physics, 99(A12), 23661-23671.
427 LeDocq, M. J., Gurnett, D. A., & Hospodarsky, G. B. (1998). Chorus source locations from VLF
428 Poynting flux measurements with the Polar spacecraft. Geophysical Research Letters, 25(21),
429 4063-4066.
430 Loi, S. T., Murphy, T., Cairns, I. H., Menk, F. W., Waters, C. L., Erickson, P. J., ... & Offringa,
431 A. R. (2015). Real-time imaging of density ducts between the plasmasphere and ionosphere.
432 Geophysical Research Letters, 42(10), 3707-3714.
433 Li, W., Ni, B., Thorne, R. M., Bortnik, J., Green, J. C., Kletzing, C. A., ... & Hospodarsky, G. B.
434 (2013). Constructing the global distribution of chorus wave intensity using measurements of
435 electrons by the POES satellites and waves by the Van Allen Probes. Geophysical Research
436 Letters, 40(17), 4526-4532.
437 Maxworth, A. S., Gołkowski, M., Malaspina, D. M., & Jaynes, A. N. (2020). Raytracing Study
438 of Source Regions of Whistler Mode Wave Power Distribution Relative to the Plasmapause.
439 Journal of Geophysical Research: Space Physics, 125(4), e2019JA027154.
440 Mozer, F. S., Agapitov, O. V., Blake, J. B., & Vasko, I. Y. (2018). Simultaneous Observations of
441 Lower Band Chorus Emissions at the Equator and Microburst Precipitating Electrons in the
442 Ionosphere. Geophysical Research Letters, 45(2), 2017GL076120.

443 Ni, B., Thorne, R. M., Shprits, Y. Y., & Bortnik, J. (2008). Resonant scattering of plasma sheet
444 electrons by whistler-mode chorus: Contribution to diffuse auroral precipitation. Geophysical
445 Research Letters, 35(11).
446 Nishimura, Y., Bortnik, J., Li, W., Thorne, R. M., Lyons, L. R., Angelopoulos, V., ... & Ergun,
447 R. (2010). Identifying the driver of pulsating aurora. science, 330(6000), 81-84.
448 Nishimura, Y., Bortnik, J., Li, W., Thorne, R. M., Chen, L., Lyons, L. R., ... & Cully, C. (2011).
449 Multievent study of the correlation between pulsating aurora and whistler mode chorus
450 emissions. Journal of Geophysical Research: Space Physics, 116(A11).
451 Nunn, D. (1974). A self-consistent theory of triggered VLF emissions. Planetary and Space
452 Science, 22(3), 349-378.
453 Omura, Y., Katoh, Y., & Summers, D. (2008). Theory and simulation of the generation of
454 whistler-mode chorus. Journal of Geophysical Research: Space Physics, 113(A4).
455 Omura, Y., Hikishima, M., Katoh, Y., Summers, D., & Yagitani, S. (2009). Nonlinear
456 mechanisms of lower-band and upper-band VLF chorus emissions in the magnetosphere.
457 Journal of Geophysical Research: Space Physics, 114(A7).
458 Pollock, C., Moore, T., Jacques, A., Burch, J., Gliese, U., Saito, Y., ... & Dorelli, J. (2016). Fast
459 plasma investigation for magnetospheric multiscale. Space Science Reviews, 199(1-4), 331-
460 406.
461 Russell, C. T., Anderson, B. J., Baumjohann, W., Bromund, K. R., Dearborn, D., Fischer, D., ...
462 & Means, J. D. (2016). The magnetospheric multiscale magnetometers. Space Science
463 Reviews, 199(1-4), 189-256.
464 Santolík, O., & Gurnett, D. A. (2003). Transverse dimensions of chorus in the source region.
465 Geophysical Research Letters, 30(2), 1031.
466 Santolik, O., Gurnett, D. A., & Pickett, J. S. (2004). Multipoint investigation of the source region
467 of storm-time chorus. In Annales Geophysicae (Vol. 22, pp. 2555–2563).
468 Santolík, O., Gurnett, D. A., Pickett, J. S., Chum, J., & Cornilleau-Wehrlin, N. (2009). Oblique
469 propagation of whistler mode waves in the chorus source region. Journal of Geophysical
470 Research: Space Physics, 114(A12).
471 Santolík, O., Pickett, J. S., Gurnett, D. A., Menietti, J. D., Tsurutani, B. T., & Verkhoglyadova,
472 O. (2010). Survey of Poynting flux of whistler mode chorus in the outer zone. Journal of
473 Geophysical Research: Space Physics, 115(A7).

Santolík, O., Kletzing, C. A., Kurth, W. S., Hospodarsky, G. B., & Bounds, S. R. (2014). Fine structure of large-amplitude chorus wave packets. Geophysical Research Letters, 41(2), 293-299.

Shen, X.-C., Li, W., Ma, Q., Agapitov, O., & Nishimura, Y. (2019). Statistical Analysis of Transverse Size of Lower Band Chorus Waves Using Simultaneous Multisatellite Observations. Geophysical Research Letters, 46(11), 5725–5734.

Shumko, M., Sample, J., Johnson, A., Blake, B., Crew, A., Spence, H., et al. (2018). Microburst Scale Size Derived From Multiple Bounces of a Microburst Simultaneously Observed With the FIREBIRD-II CubeSats. Geophysical Research Letters, 45(17), 8811–8818.

Shumko, M., Johnson, A. T., Sample, J. G., Griffith, B. A., Turner, D. L., O'Brien, T. P., ... & Claudepierre, S. G. (2020). Electron Microburst Size Distribution Derived With AeroCube-6. Journal of Geophysical Research: Space Physics, 125(3), e2019JA027651.

Smith, R. L., & Angerami, J. J. (1968). Magnetospheric properties deduced from OGO 1 observations of ducted and nonducted whistlers

Sonwalkar, V. S., Inan, U. S., Bell, T. F., Helliwell, R. A., Chmyrev, V. M., Sobolev, Y. P., ... & Selegej, V. (1994). Simultaneous observations of VLF ground transmitter signals on the DE 1 and COSMOS 1809 satellites: Detection of a magnetospheric caustic and a duct. Journal of Geophysical Research: Space Physics, 99(A9), 17511-17522.

Sonwalkar, V. S. (2006). The influence of plasma density irregularities on whistler-mode wave propagation. In Geospace electromagnetic waves and radiation (pp. 141-190). Springer, Berlin, Heidelberg.

Sonwalkar, V. S., Carpenter, D. L., Reddy, A., Proddaturi, R., Hazra, S., Mayank, K., & Reinisch, B. W. (2011). Magnetospherically reflected, specularly reflected, and backscattered whistler mode radio-sounder echoes observed on the IMAGE satellite: 1. Observations and interpretation. Journal of Geophysical Research: Space Physics, 116(A11).

Stix, T. H. (1992). Waves in Plasmas AIP. New York.

Streltsov, A. V., Lampe, M., Manheimer, W., Ganguli, G., & Joyce, G. (2006). Whistler propagation in inhomogeneous plasma. Journal of Geophysical Research: Space Physics, 111(A3).

Streltsov, A. V., Lampe, M., & Ganguli, G. (2007). Whistler propagation in nonsymmetrical density channels. Journal of Geophysical Research: Space Physics, 112(A6).

505 Sudan, R. N., & Ott, E. (1971). Theory of triggered VLF emissions. Journal of Geophysical
506 Research, 76(19), 4463-4476.
507 Taflove, A., & Hagness, S. C. (2005). Computational electrodynamics: the finite-difference time-
508 domain method. Artech house.
509 Thomson, R. J. (1978). The formation and lifetime of whistler ducts. Planetary and Space
510 Science, 26(5), 423–430.
511 Thorne, R. M. (2010). Radiation belt dynamics: The importance of wave-particle interactions.
512 Geophysical Research Letters, 37(22).
513 Torbert, R. B., Russell, C. T., Magnes, W., Ergun, R. E., Lindqvist, P. A., LeContel, O., ... &
514 Needell, J. (2016). The FIELDS instrument suite on MMS: Scientific objectives,
515 measurements, and data products. Space Science Reviews, 199(1-4), 105-135.
516 Tsurutani, B. T., & Smith, E. J. (1974). Postmidnight chorus: A substorm phenomenon. Journal
517 of Geophysical Research, 79(1), 118-127.
518 Woodroffe, J. R., Streltsov, A. V., Vartanyan, A., & Milikh, G. M. (2013). Whistler propagation
519 in ionospheric density ducts: Simulations and DEMETER observations. Journal of
520 Geophysical Research: Space Physics, 118(11), 7011-7018.
521 Woodroffe, J. R., & Streltsov, A. V. (2014). Whistler interaction with field-aligned density
522 irregularities in the ionosphere: Refraction, diffraction, and interference. Journal of
523 Geophysical Research: Space Physics, 119(7), 5790-5799.
524 Yoon, P. H. (2011). Large-amplitude whistler waves and electron acceleration. Geophysical
525 research letters, 38(12).
526 Zhang, X. J., Agapitov, O., Artemyev, A. V., Mourenas, D., Angelopoulos, V., Kurth, W. S., ...
527 & Hospodarsky, G. B. (2020). Phase Decoherence Within Intense Chorus Wave Packets
528 Constrains the Efficiency of Nonlinear Resonant Electron Acceleration. Geophysical
529 Research Letters, e2020GL089807.

Figure 1.

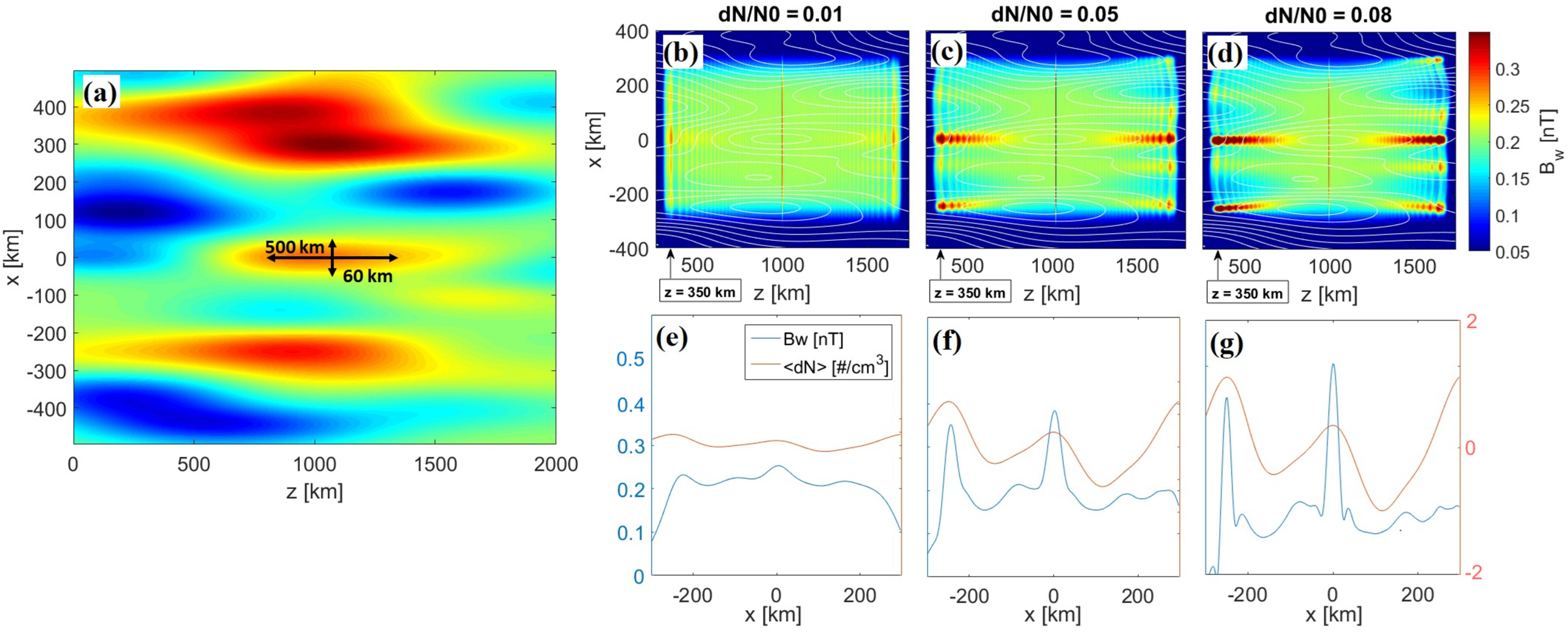
(a)
500 km
60 km
x [km]
z [km]
dN/N0 = 0.01
dN/N0 = 0.05
dN/N0 = 0.08
(b)
(c)
(d)
z = 350 km
B_w [nT]
(e)
(f)
(g)
Bw [nT]
<dN> [#/cm^3]

Figure 2.

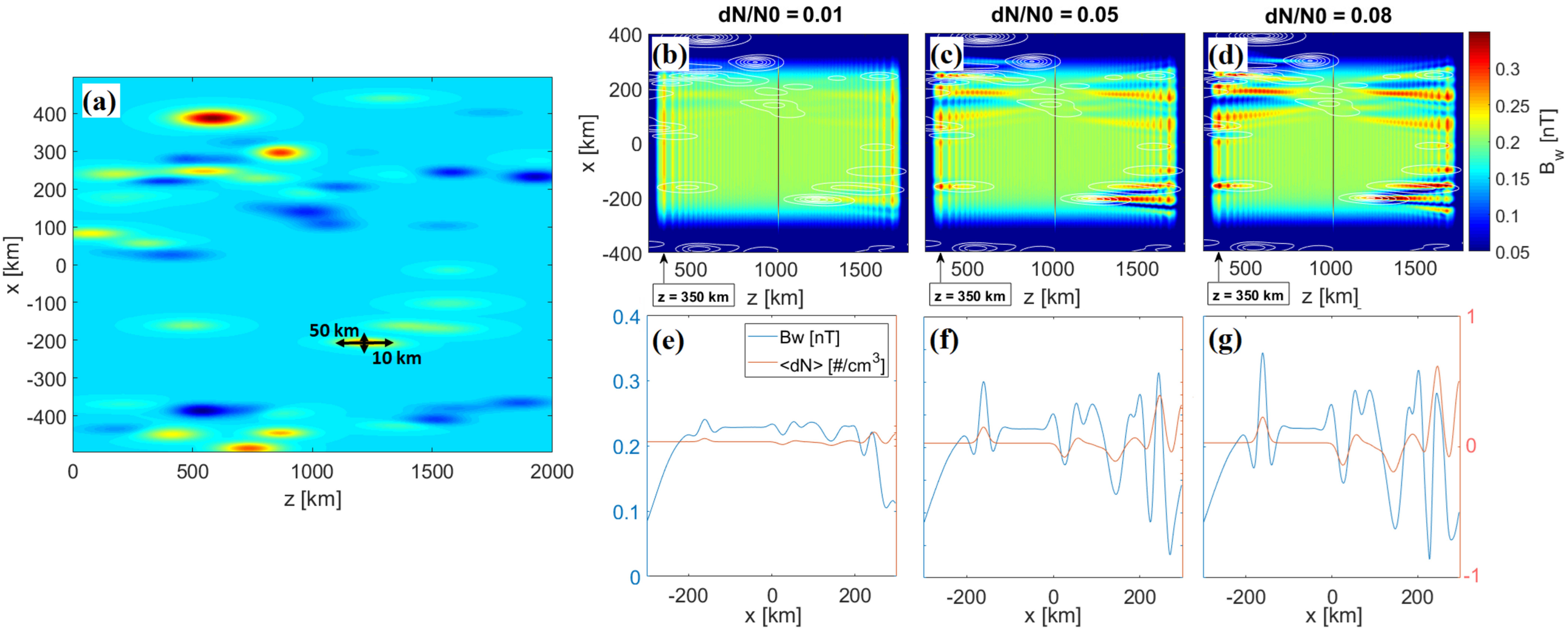
(a)
50 km
10 km
x [km]
z [km]
dN/N0 = 0.01
dN/N0 = 0.05
dN/N0 = 0.08
(b)
(c)
(d)
z = 350 km
B_w [nT]
(e)
(f)
(g)
Bw [nT]
<dN> [#/cm^3]

Figure 3.

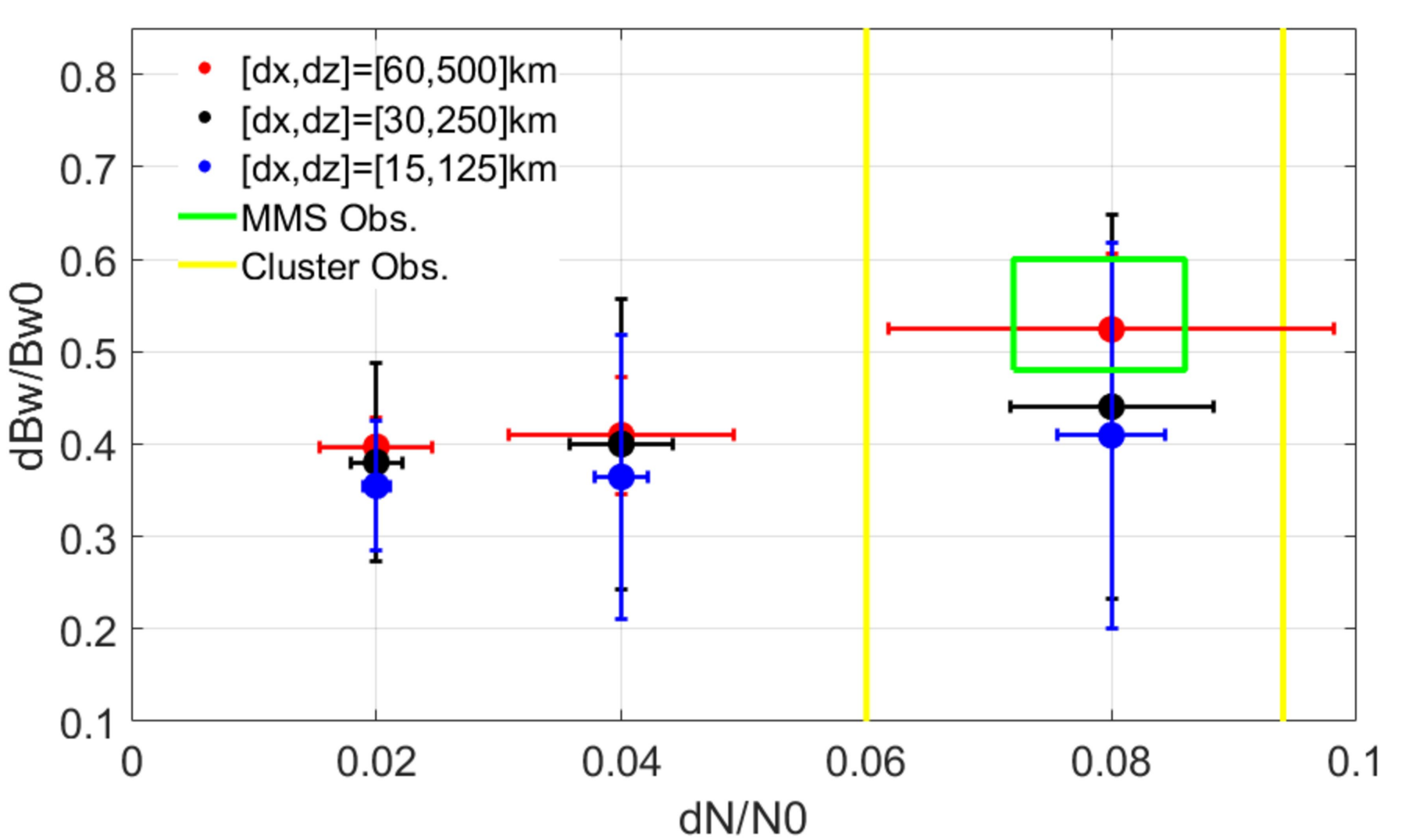
[dx,dz]=[60,500]km
[dx,dz]=[30,250]km
[dx,dz]=[15,125]km
MMS Obs.
Cluster Obs.
dBw/Bw0
dN/N0
0.8
0.7
0.6
0.5
0.4
0.3
0.2
0.1
0
0.02
0.04
0.06
0.08
0.1

Figure 4.

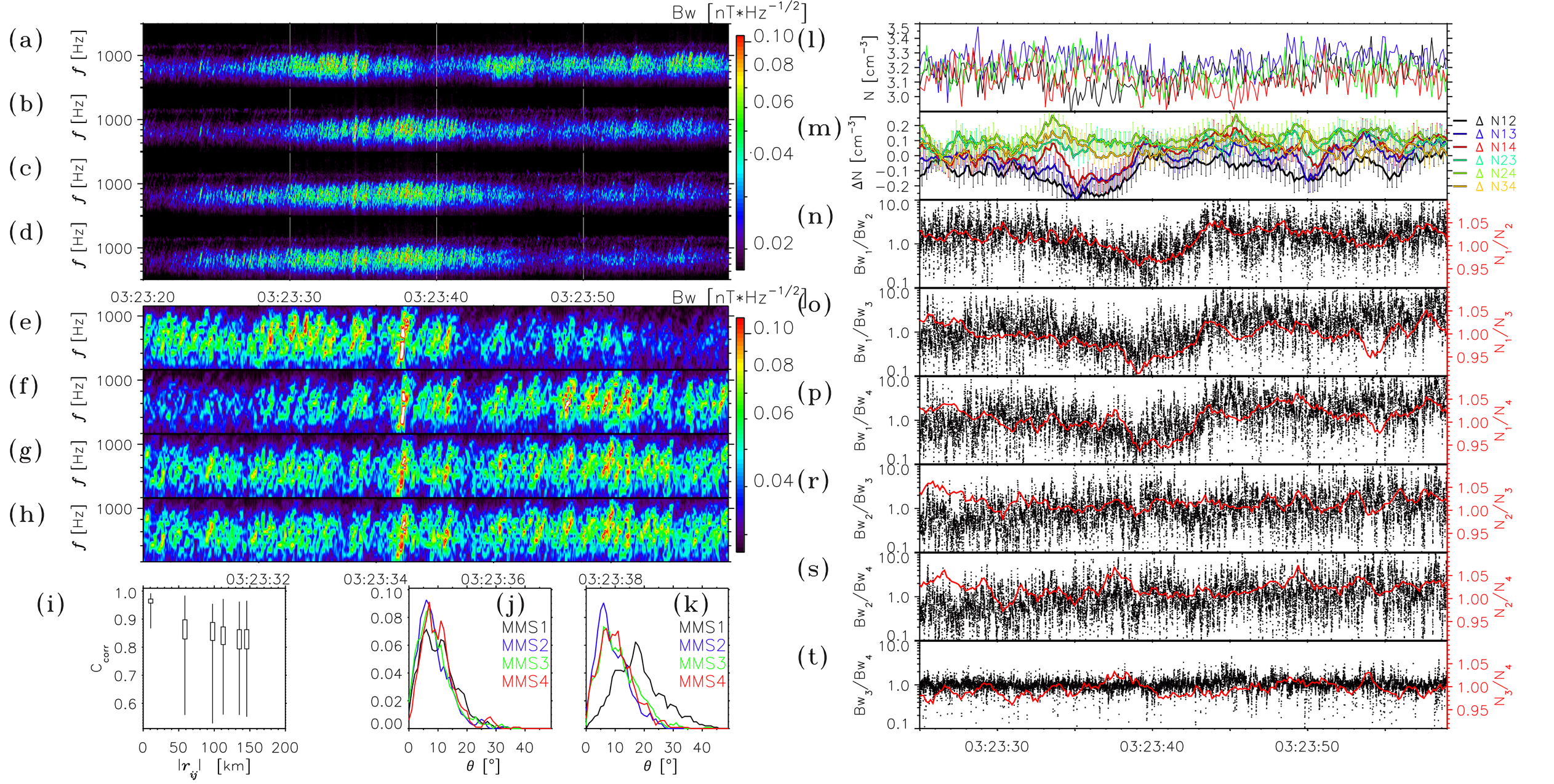
(a)
(b)
(c)
(d)
(e)
(f)
(g)
(h)
(i)
(j)
(k)
(l)
(m)
(n)
(o)
(p)
(r)
(s)
(t)
f [Hz]
1000
Bw [nT*Hz$^{-1/2}$]
0.10
0.08
0.06
0.04
0.02
03:23:20
03:23:30
03:23:40
03:23:50
03:23:32
03:23:34
03:23:36
03:23:38
C_{corr}
$|r_{ij}|$ [km]
θ [°]
MMS1
MMS2
MMS3
MMS4
N [cm^{-3}]
ΔN [cm^{-3}]
Δ N12
Δ N13
Δ N14
Δ N23
Δ N24
Δ N34
Bw_1/Bw_2
Bw_1/Bw_3
Bw_1/Bw_4
Bw_2/Bw_3
Bw_2/Bw_4
Bw_3/Bw_4
N_1/N_2
N_1/N_3
N_1/N_4
N_2/N_3
N_2/N_4
N_3/N_4